Investigate the Effects of the Laser Cladding Parameters on the Microstructure, Phases Formation, Mechanical and Corrosion Properties of Metallic Glasses Coatings for Biomedical Implant Application

Mahmoud Z. Ibrahim, Ahmed A. D. Sarhan, M. O. Shaikh, T. Y. Kuo, Farazila Yusuf, and M. Hamdi

1 Introduction

Metallic glasses (MG) or amorphous metals are the description of non-crystalline metals. Conventionally, metals tend to form crystalline structure during transition from liquid to solid state. For MG, the atoms are randomly arranged in the matrix showing no crystals or no ordered-arrangement of atoms [3]. In Fig. 1, a scanning electron microscope (SEM) image showing the difference between the amorphous and crystalline phases of Zr-based MG sample, and Fig. 2 shows the corresponding X-ray diffraction pattern (XRD) [4]. The MG systems have superior mechanical properties and promising tribological and corrosion resistance ability [5]. These superior properties are owing to the homogeneous single phase structure (amorphous structure), no grain boundaries, no dislocations and other crystal defects [5–7].

M. Z. Ibrahim
Centre of Advanced Manufacturing and Material Processing, Department of Mechanical Engineering, Faculty of Engineering, University of Malaya, Kuala Lumpur, Malaysia

Department of Mechanical Engineering, Southern Taiwan University of Science and Technology, Taiwan, Republic of China

Department of Mechanical Engineering, Faculty of Engineering, Ain Shams University, Cairo, Egypt

A. A. D. Sarhan (✉)
Department of Mechanical Engineering, King Fahd University of Petroleum and Minerals, Dhahran, Saudi Arabia
e-mail: ahsarhan@kfupm.edu.sa

M. O. Shaikh · T. Y. Kuo
Department of Mechanical Engineering, Southern Taiwan University of Science and Technology, Taiwan, Republic of China

F. Yusuf · M. Hamdi
Centre of Advanced Manufacturing and Material Processing, Department of Mechanical Engineering, Faculty of Engineering, University of Malaya, Kuala Lumpur, Malaysia

B. AlMangour (ed.), *Additive Manufacturing of Emerging Materials*,
https://doi.org/10.1007/978-3-319-91713-9_10

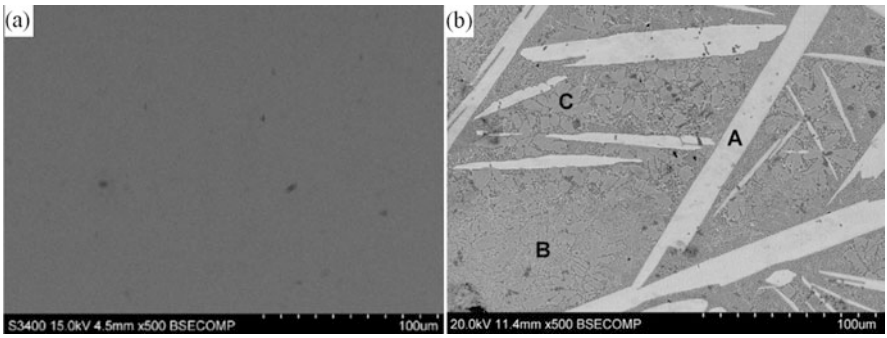

Fig. 1 SEM image of Zr-based MG (**a**) full amorphous phase, (**b**) Combined amorphous phase (A) with crystalline phases (B,C) [4]

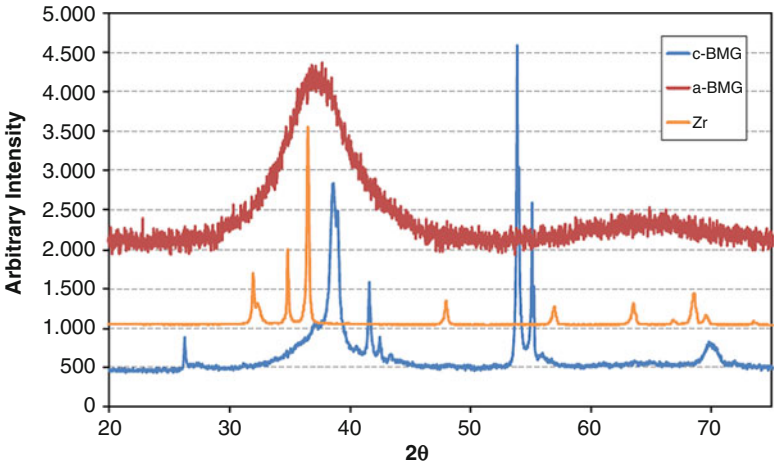

Fig. 2 XRD pattern of three different Zr alloy sample, Red: full amorphous phase, Blue: combined amorphous and crystalline phases, Orange: full crystalline phase

1.1 Evolution of MG

In 1960, the first MG was proposed. The MG was produced under super cooling rates (cooling rate reached 10^6 K/s) to preserve the amorphous structure of liquid metal. Because of the challenging requirements of the excessive cooling rates, only thin ribbons (~10 μm) and limited dimensions could be produced [3]. Chen and Turnbull performed detailed investigations on the crystallization process of MG and later they succeeded to extend the critical thickness of the MG castings to 1 mm [8].

Further researcher focused on increasing the critical casting thickness of the MG until Peker and Johnson introduced Vitreloy 1 (Zr41.2Ti13.8Cu12.5Ni10Be22.5) with high glass forming ability (GFA) at relatively low cooling rates (10 K/s or less)

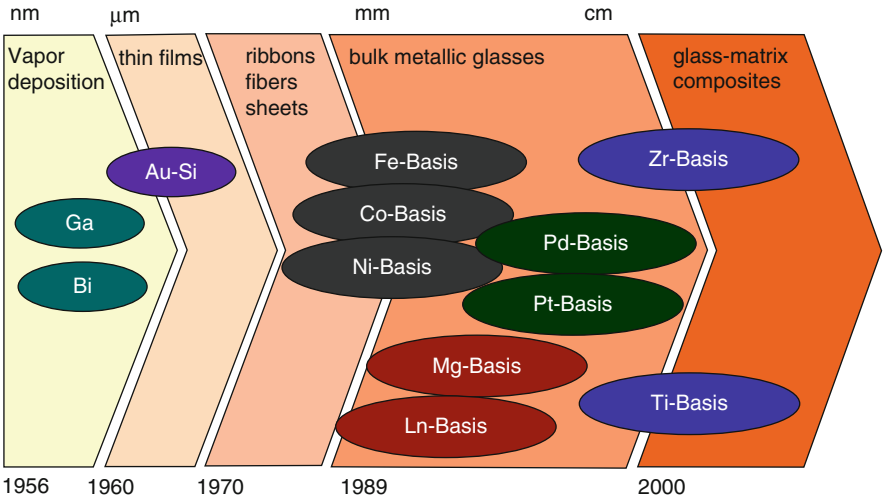

Fig. 3 Historic advances in MG systems [11]

[9]. Recent researches reported that higher GFA can be achieved (from 0.1 K/s to 100 K/s) by applying the following rules; (1) multicomponent MG system (three or more elements), (2) significant differences in the atomic sizes of the main elements, (3) deep eutectics in the phase diagram of the alloys, (4) large difference between the glass transition temperature (T_g) and crystallization temperature (T_x) [10]. These rules enabled the fabrication of larger MG objects (up to few centimeters) and emerged them in structural applications. Figure 3 shows the development of MG systems in last few decades.

For various applications and different industries, different metal-based MG systems were proposed. The most common MG systems are the Fe, Zr, Ti, Co, Ni, Pt, Mg, Pd and Cu-based MG. Figure 4 shows the maximum diameter – which can represent the GFA – of different MG systems that can be fabricated with the corresponding discovery year [12].

1.2 Mechanical Properties of MG

As mentioned above, MG exhibits superior mechanical properties and tribological and corrosion characteristics compared to the conventional known crystalline metallic alloys. Because of the excellent corrosion resistance of MG and proved biocompatibility, MG is considered a promising candidate for biomedical application [13]. The mechanical properties of common MG systems in biomedical applications are stated in Table 1. It is noted that MG systems exceeds the mechanical properties of the common metallic alloys. It is worth mentioning that Zr-based MG showed

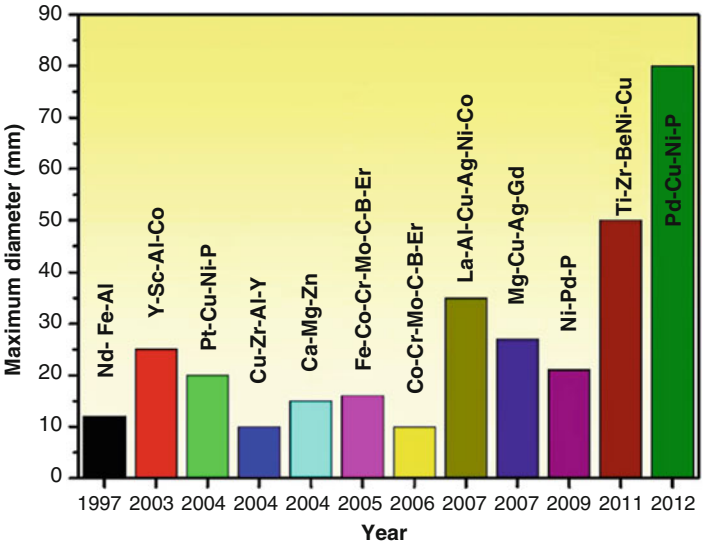

Fig. 4 Different MG systems with the corresponding maximum diameter and discovered year [12]

Table 1 Mechanical properties of common biomedical MG systems compared to the most popular biomedical metallic alloys [2, 13, 14]

Material	Critical diameter, mm	Compressive strength/ (UTS), MPa	Young's modulus	Vickers's hardness, H_v (HRC)
Ti-alloy		(241–896)	40–115	(30–39)
Co-alloy		(650–1900)	200–240	(40–47)
Stainless steel		(490–1700)	200–220	(25–50)
Ti-based MG	2–5	1200–2640	80–119	530–816
Zr-based MG	3–20	1450–2158	68–102	411–590
Fe-based MG	2–16	2500–4200	176–220	845–1253
Ca-based MG	0.9–6	364–600	19.4–46	0.7–1.42
Mg-based MG	0.025–6	550–848	35–66	2.16–4 GPa
Cortical bone		50–150	1–20	

promising GFA which allow fabrication of larger objects, and in the other side, Ti-based MG has the lowest GFA. This results in high potential to apply Zr-based and Fe-based in biomedical implants. However, biodegradable MG (Ca- and Mg-based MG) has lower Young's modulus close to the cortical bone which reduce the

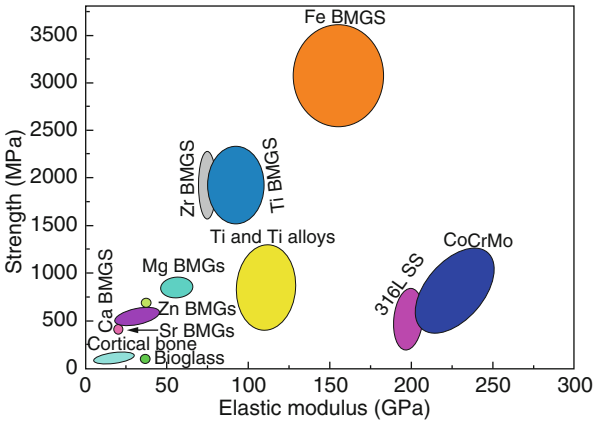

Fig. 5 Graph comparing the different metallic alloys and MG used in biomedical applications

effect of stress shielding, but they exhibit relatively low strength compared to the other MG systems. This brings such MG to more investigation to ensure durability and acceptable performance when implanted. Figure 5 shows graphical comparison between the different metallic alloys and MG used in biomedical applications.

Generally, all MG suffer from brittleness and low toughness compared to crystalline alloys. This drawback hinders the application of MG and represent challenging for fabricating MG. So, great effort was focused on toughening MG through developing mixed structure (amorphous structure with dendrite crystalline structure). This mixed structure – usually called dendrite reinforced amorphous composite – can enhance the Poisson's ratio and the increase the compressive ductility by 30%, [15]. These advances promote the applications of MG in biomedical implants products (Fig. 6).

1.3 Biocompatibility of MG Systems

According to D. Williams, biocompatibility is defined as "the ability of a biomaterial to perform its desired function with respect to a medical therapy, without eliciting any undesirable local or systemic effects in the recipient or beneficiary of that therapy, but generating the most appropriate beneficial cellular or tissue response in that specific situation, and optimizing the clinically relevant performance of that therapy" [16]. From this definition, a biocompatible material should meet the following requirements;

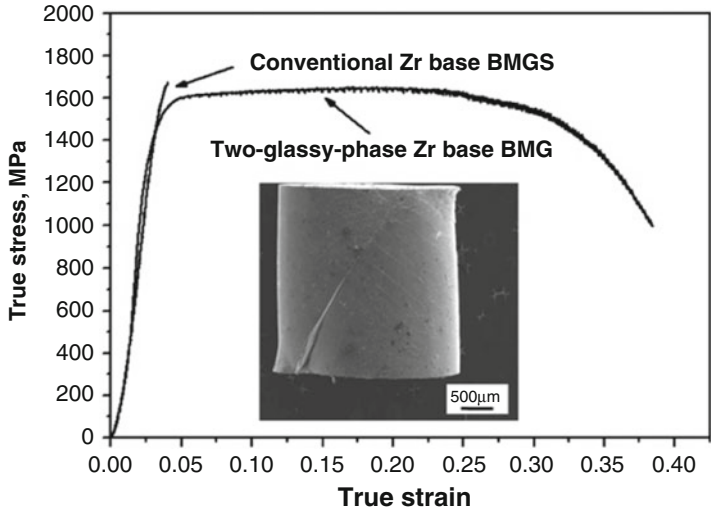

Fig. 6 Enhancement of compressive strain of Zr-based MG [15]

1. High corrosion resistance, the material should exhibit lower ion release within the hosting body, so reduce the hazardous effect of released ions, and hence, prevent further side-effects of these ions.
2. Non-toxic, the material is not considered as cytotoxic, in other words, the material used is not destroying cells and living tissues in contact
3. Allergy-free, the material should be accepted by the hosting body without irritation or inflammation.
4. Suitable mechanical properties, to be able to withstand the conditions of different loadings during operation.
5. And acceptable osteointegration, in terms of ability to bond with the living tissue.

Generally, metallic alloys were considered to have acceptable biocompatibility. However, all the developed metallic alloys failed to show excellent durability in bone-implants applications. In the other side, MG systems proved to be an excellent substitute of conventional metallic alloys.

Generally, most of the MG systems exhibit high corrosion resistance due to the single glassy phase as mentioned above [7]. X. Lan et al. reported the enhanced tribological properties of Ti-based MG specially after the addition of Sn. The results showed high hardness values which indicate excellent wear resistance [17]. A cytotoxicity evaluation study revealed the excellent biocompatibility of Fe-based MG and revealed the promising potential in bone-implants and dental applications, [18]. Many other studies proved the excellent biocorrosion properties of MG and their potential in different biomedical applications [19–22] (Fig. 7).

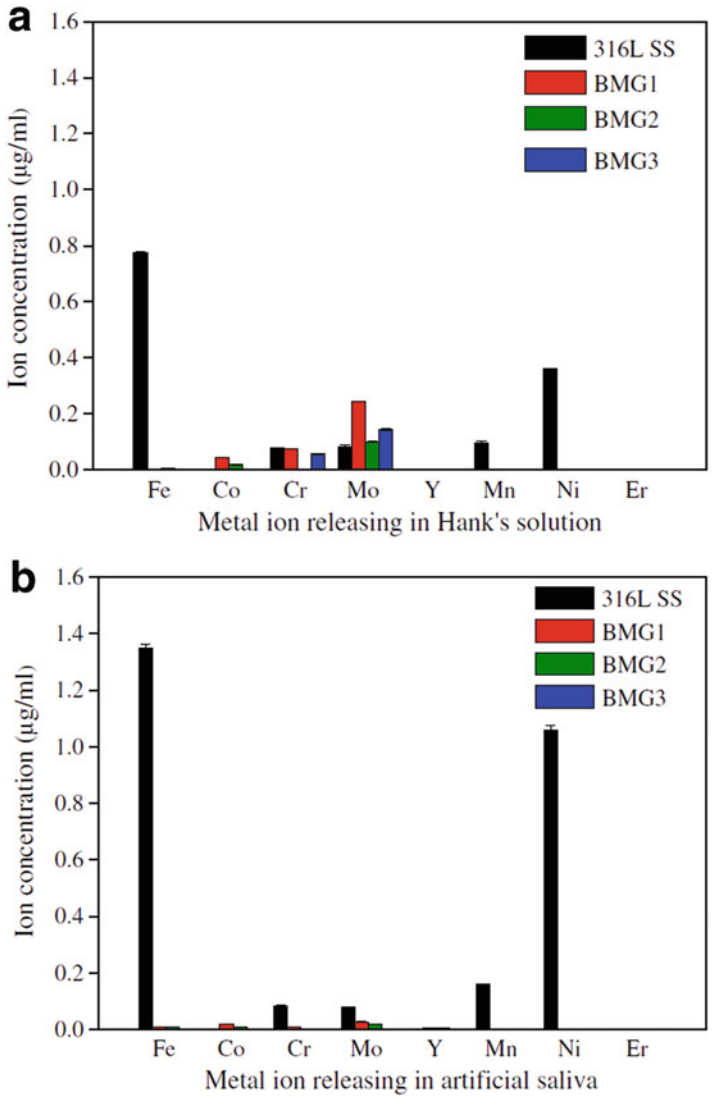

Fig. 7 Ion-release of three different Fe-based MG and 316 L SS in (**a**) Hank's solution, (**b**) artificial saliva [18]

2 Techniques to Fabricate MG

Different techniques were developed to fabricate metallic glass objects. These techniques were subjected to exhibit rapid cooling sufficient to form the amorphous structure. Starting from micron-sized thickness ribbons to cylinders with few

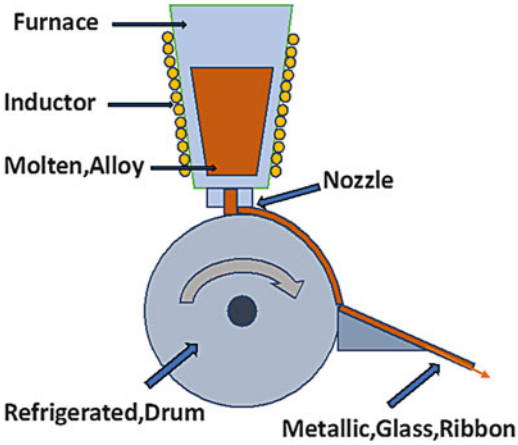

Fig. 8 Melt spinning technique to produce MG ribbon [25]

centimeters in diameter, researchers succeeded to develop many fabrication techniques to produce MG products. GFA of available MG systems still lack to produce larger size products. This limitation represents a challenging research area for further emerging MG in more applications.

In this section, different available MG production techniques are discussed.

2.1 Melt Spinning

Melt spinning is the most common technique to produce high quality amorphous ribbons. This technique is able to produce continuous thin ribbon (20–30 μm) with different widths. This technique is based on injecting molten metal through certain nozzle onto rotating wheel. The wheel is made from copper, so it allows rapid solidification of the molten metal forming very thin ribbon. This technique can achieve more than 10^5 K/s cooling rate [23].

Different parameters affect the quality and thickness of produced ribbons. Wheel rotating speed, melt temperature, injecting gas pressure, and nozzle-wheel gap are the main parameters. It was reported that smaller gap results in better surface quality of ribbons and hence, higher degree of amorphous structure [24] (Fig. 8).

2.2 Casting

Typical casting of MG using water-cooled copper molds is commonly used to produce MG ingots. The process is based on melting the MG in inert gas atmosphere – to prevent further oxidations – using electric arc, then inject the melt into copper

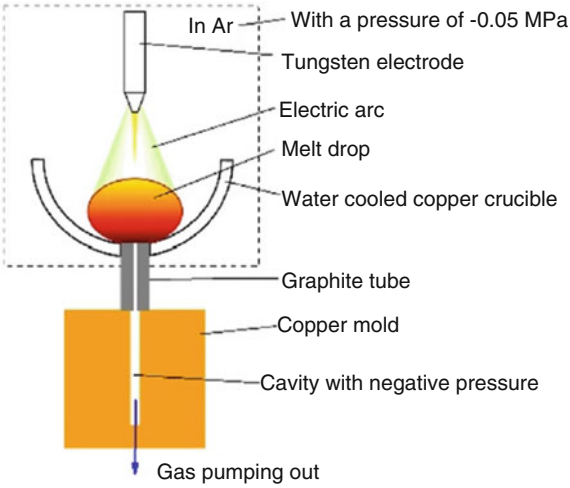

Fig. 9 Copper-mold injection casting used for MG production

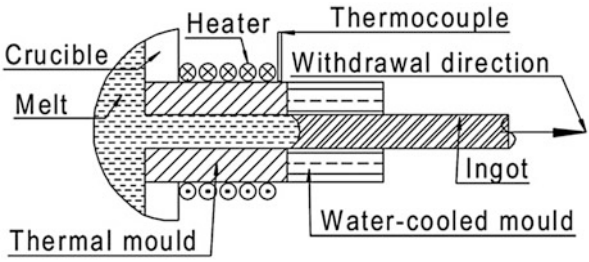

Fig. 10 Schematic of continuous casting system proposed by T. Zhang et al

mold through negative gas pressure. The copper mold facilitates high cooling rates sufficient for glassy phase formation [26]. Figure 9 shows schematic of copper-mold casting technique.

T. Zhang et al. developed a novel technique for continuous casting of MG. The authors succeeded to produce Zr-based MG rod with 10 mm diameter rod and several tens centimeters long. The authors proposed horizontal continuous casting system equipped with water-cooled mold at the exit as shown in Fig. 10 [27].

2.3 Additive Manufacturing

Additive manufacturing (AM) – or 3D printing – propose fabrication technique based on adding successive layers to build objects. The process is categorized into three categories: powder-based, liquid-based and solid-based [28]. The powder and solid-based process can be used for almost all materials, while the liquid-based is limited to certain photosensitive polymers. However, powder-based and liquid-

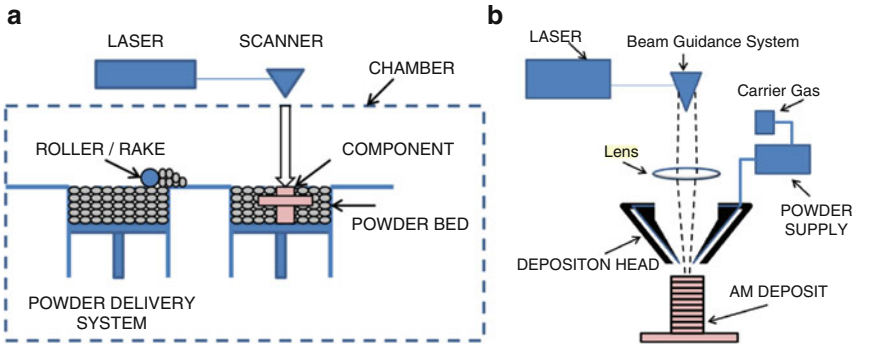

Fig. 11 Principle of (**a**) Selective Laser Melting (SLM), and (**b**) Laser Engineering Net Shaping [32]

based are attracting more attention because of higher accuracy and precision. AM has become of great interest because of their relatively lower cost – compared to conventional manufacturing techniques – flexibility, and ability to produce complex objects in shorter times [29].

In 1980's, rapid prototyping was introduced as the first form of AM technology. The proposed technique was developed to produce 3D objects using CAD software. This technology facilitated the implementation of complex designs with low cost and in short time. Later, stereolithography was developed employing polymer resin that solidify under UV laser beam. Recently, the AM is developing and extending to more advanced applications as aerospace, automotive, biomedical, etc. that requires materials with higher mechanical properties [30].

Commonly, AM utilizes laser energy to melt and sinter printing material during building the model. Selective laser melting (SLM), laser engineering net shaping (LENS) and electron beam melting (EBM) are the common techniques for AM. These methods can process metals, polymers, ceramics or blend of them.

SLM is based on employing laser beam to melt and sinter powder layer with specified path spread on a piston. The piston movement – upward – determines the layer thickness and excessive powder is removed by the end of process [31]. In the other side, LENS inject material powder into the melting pool, so no removal of excessive powder is needed, Fig. 11 shows the principle of SLM and LENS process.

In EBM method, an electron laser beam powered with high voltage (30–60 kV) in a vacuumed chamber to avoid oxidation. The process uses two magnetic coils to focus and deflect the electron beam respectively (Fig. 12).

2.3.1 Laser Cladding Technique for MG Coatings

Laser cladding is another technique of AM where a single or multiple layer of material is developed on the surface of substrate. The key advantage of laser cladding is the strong metallurgical bond built between the successive layers. This

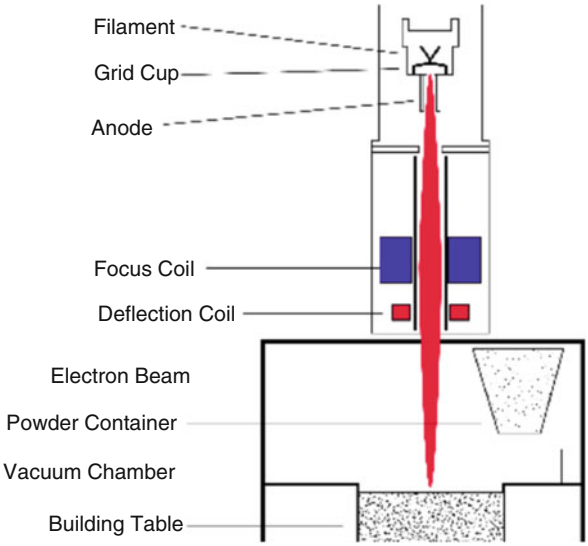

Fig. 12 Schematic showing the EBM setup and principle [33]

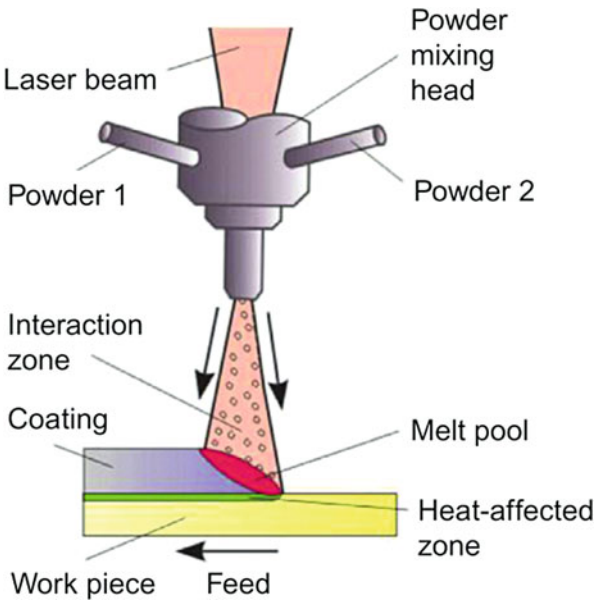

Fig. 13 Powder-feed laser cladding technique [34]

leads to dense structure of the coating with excellent mechanical properties. The metallurgical bond is built as the laser beam penetrates the layer and the substrate, allowing dilution take place at the interface [34]. In addition, laser cladding offers versatile and productive method, besides it can be utilized to repair expensive metallic parts [35] (Fig. 13).

Table 2 Elemental composition of ASTM F2229 substrate

Material	Fe	Cr	Ni	Mo	Mn	Si	Cu	N	C	P	S
ASTM F2229	Balance	20.00	0.10	21.00	1.00	0.75	0.25	0.90	0.08	0.03	0.01

Laser cladding can work with powder-bed or powder-feed technique. The results proved that both techniques do not affect the resulted coating layer [36]. The parameters affecting the properties of the coating layer are laser power, scanning speed, laser beam spot size, layer thickness and the overlap percentage [37, 38].

An important factor for the amorphous structure is the cooling rate. A critical cooling rate is defined for each MG system depending on the composition and the stability of the MG. As laser cladding offers high cooling rate, but it is important to control the laser parameters to maintain the amorphous phase. An experiment was performed to investigate the effect of the laser parameters on the properties of laser cladded MG.

2.3.2 Experimental Procedures

Sample Preparation

Substrate samples of 30 × 30 mm are prepared from 3 mm ASTM F2229 stainless-steel sheet. The respective elemental composition is listed in Table 2. The coating material is Fe-based amorphous powder (Fe-Cr-Mo-B-C) with normally distributed particle size 20–70 μm. The samples were sand blasted using 40-grit alumina particles, then cleaned in ultrasonic bath using DI-water then ethanol to remove dirt and contaminations on the surface.

The powder was preplaced – the dry powder is spread on the surface then ethanol is added and put the sample in ultrasonic bath to ensure uniform distribution of powder on the surface, then dried using hair dryer – using 0.22 g/cm^2 spread rate, Fig. 14.

The cladding was done using diode laser machine – LDF 4000–60 maximum power 4.4 kW, wavelength 978–1025 ± 10 nm, LaserLine, Germany – under Ar gas environment to prevent further oxidation of the coating layer following the parameters levels in Table 3. Three parameters were selected for the study; laser power, spot size and scanning speed. Three levels of each parameter were chosen to investigate the effect of each parameter on the resulted microstructure, phases formation, hardness and the corrosion resistance of the Fe-based MG coating. The selected parameters levels are based on the preliminary experiments held.

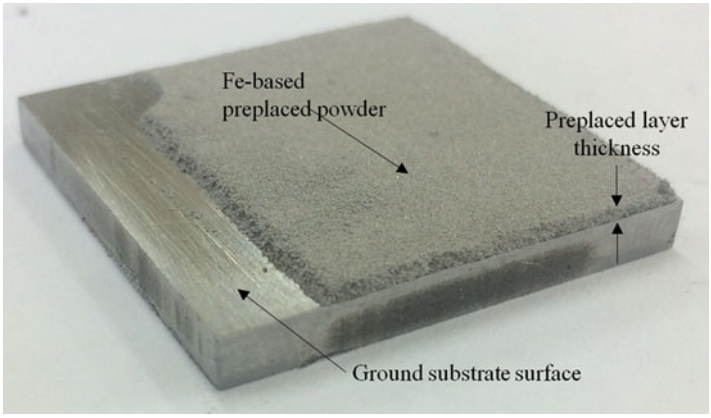

Fig. 14 Preplaced Fe-based amorphous powder

Table 3 Selected parameters to fabricate Fe-based MG coatings

Sample code	Laser power, W	Spot size, mm	Scanning speed, mm/s
A1	1500	4 × 4	15
A2	1500	4 × 4	20
A3	1500	4 × 4	25
B1	2000	4 × 4	40
B2	2000	4 × 4	45
B3	2000	4 × 4	50
D1	4000	4 × 6	30
D2	4000	4 × 6	35
D3	4000	4 × 6	40
E1	4000	4 × 8	20
E2	4000	4 × 8	25
E3	4000	4 × 8	30

Characterization and Testing

For X-ray diffraction (XRD) analysis, a sample 15 × 15 mm was cut from each sample. The surface of the coating layer was flattened using SiC 80-grit sandpaper, then ground using 150-grit to 4000-grit and polished using 40 nm alumina suspension until mirror-like surface is obtained. Then, the samples are cleaned in ultrasonic bath using DI water and ethanol. The analysis was done using Bruker D2 Phaser, Germany using Cu K_α $\lambda = 0.154060$ nm, 2θ range of 0~140° and scanning rate 3° min^{-1}.

SEM imaging (Hitachi S-3000N, Tokyo, Japan) was used to analyze the microstructure at the interface and at the coating layer, with ×1.5k magnification. The hardness measurements were taken along the cross-section at 0.1 mm distance

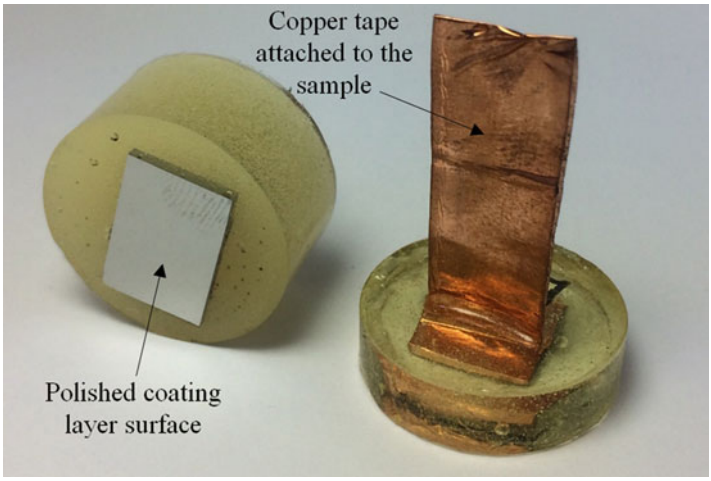

Fig. 15 Prepared sample for electrochemical corrosion test

between each successive point at 100 g testing load and 10 sec. Dwell time using Vicker's Hardness tester.

An electrochemical corrosion – Potentiodynamic polarization – test was performed in Ringer's solution (pH 7.4) as electrolyte at 37 °C to test the corrosion resistance of the Fe-based BMG coating and compare it to the bare stainless steel (Cronidur 30). The selected samples for corrosion resistance evaluation were chosen based on the best results of surface hardness, which is a measure of amorphous quality. The samples were prepared in epoxy mold as shown in Fig. 15 so the coating surface is only exposed during the test. The sample was set as working electrode (WE), Saturated Calomel Electrode (SCE) as reference electrode (RE) and platinum strip as counter electrode (CE). The open circuit potential was kept for 40–60 min until saturation attained. Then linear potential sweep was applied from −1.5 to 1.5 V with scanning rate 10 mV/s. The corrosion potential and current were obtained by Tafel extrapolation method.

2.3.3 Results

XRD Analysis

The obtained XRD patterns of the as received materials and samples are shown in Figs. 16 and 17. The analysis of XRD analysis included the analysis of multiple phases formed and the crystallinity content percentage. The crystallinity content percentage was obtained using HighScore Plus [39]. The XRD patterns showed that all samples exhibited amorphous structure – broad peak at 44° – with existence of

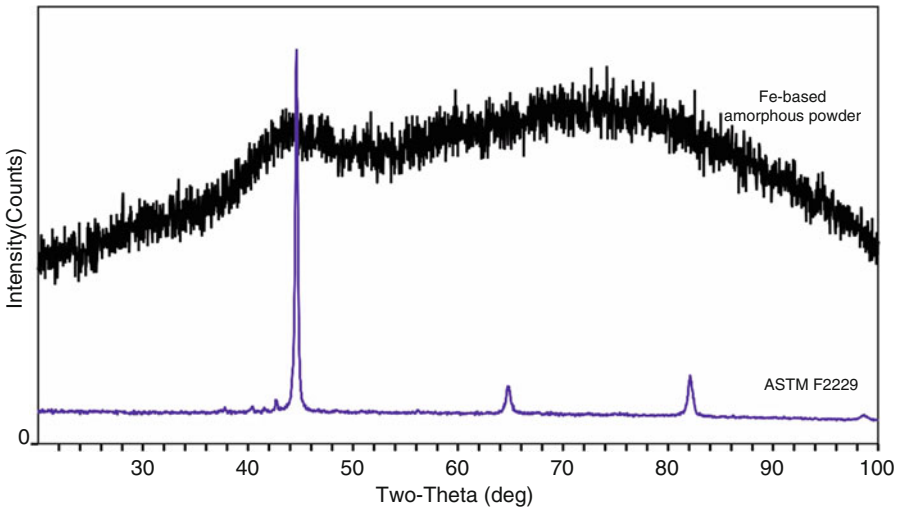

Fig. 16 XRD pattern of Fe-based amorphous powder and ASTM F2229

crystalline metallic phases as Fe, Cr and ASTM F2229 besides intermetllic compounds as iron boron (B_6Fe_{23}), chromium carbide ($Cr_{23}C_6$) and iron chromium carbide. It is noticed in sample E1, the phase iron nitride (FeN) appeared. All recognized intermetallic compounds are featured as hard and stable compounds.

It is noticed that the crystallinity content percentage around 15 $\pm$ 1%, so no significant difference between the examined samples. However, sample E1 was found to have the highest crystallinity content (18.11%). Form previous experiment, it was shown that laser power has the most significant effect on the crystallinity content. Also, the increase in scanning speed would enhance the amorphous structure in coating layer, but over-increase of scanning speed results in unsuccessful coating.

The effect of laser power on the amorphous structure of coating layer can be explained as the laser power represents the total energy transmitted to the sample per unit time, which in turn determines the temperature of the melt pool. In the other side, the scanning speed is a measure of the heating and cooling rate involved during the laser cladding process. Hence, laser power and scanning speed has an interrelation effect on the formed structure within coating layer.

The spot size is inversely proportional to the transmitted energy to the sample. In laser cladding applications, increasing spot size would enhance the coverage efficiency, but in the other side requires more power to compensate the decrease in the energy transmitted. So, power density can describe the interrelation effect between the laser power and spot size described in Eq. 1.

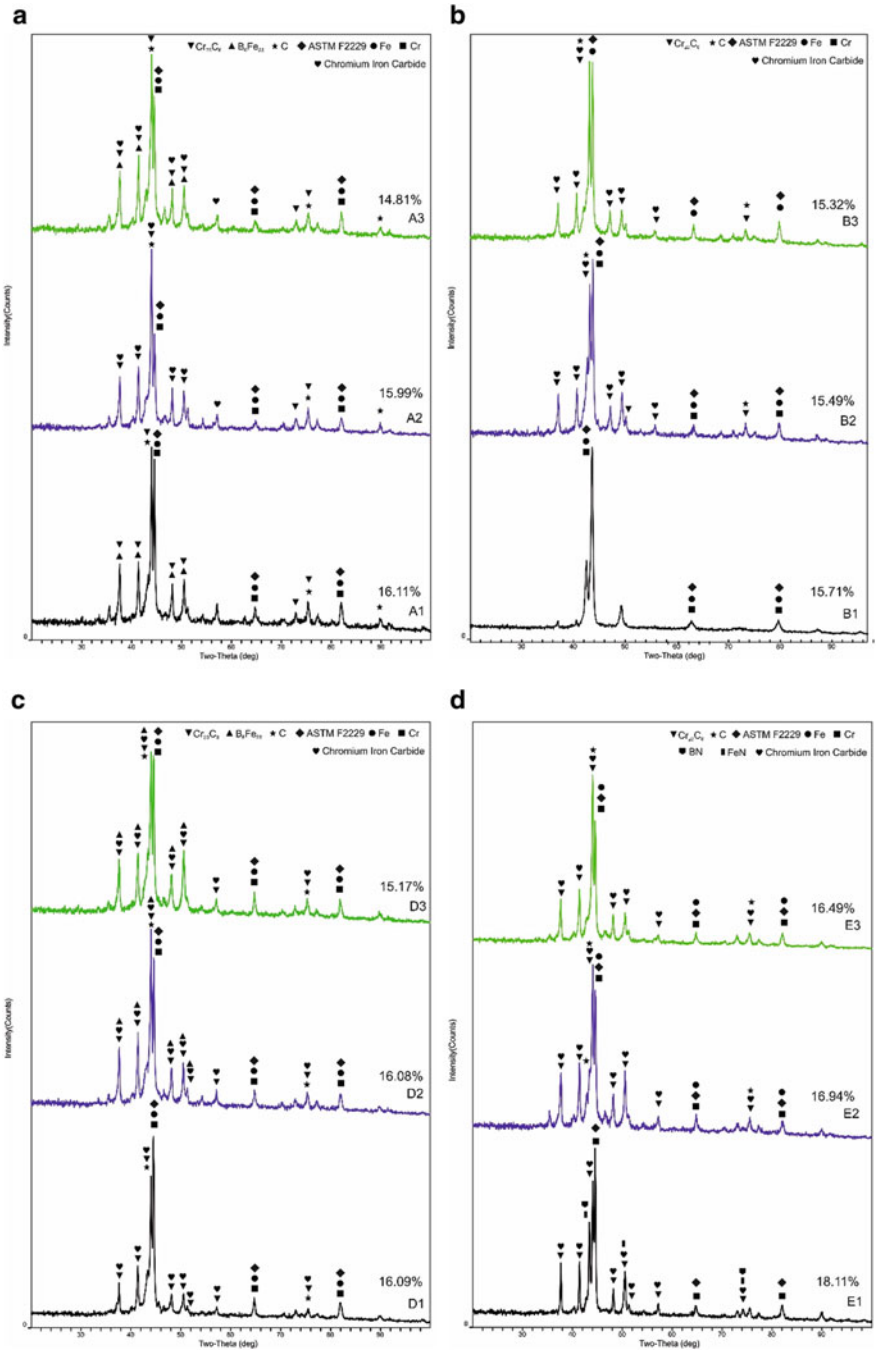

Fig. 17 XRD pattern (**a**) samples A1, A2, A3, (**b**) samples B1, B2, B3, (**c**) samples D1, D2, D3, (**d**) samples E1, E2, E3

$$\text{Power density } \left(\text{W/mm}^2\right) = \frac{\text{Power (W)}}{\text{Spot size } (\text{mm}^2)} \quad (1)$$

Based on that, sample E1 and sample B1 have the same power density with different scanning speed – 20 and 40 respectively. The XRD results revealed that sample B1 exhibited lower crystallinity (15.71%) content and the recognized phases are Fe, Cr and ASTM F2229 only, while sample E1 exhibited higher crystallinity content (18.11%) and the recognized phases are iron-nitride (FeN), $Cr_{23}C_6$ and iron chromium carbide phases. From these findings, we can conclude that scanning speed affect the crystalline phases formed, besides the crystallinity content.

It can be concluded that laser power, scanning speed and spot size have significant effect on the formed phases. In addition, the three parameters have interrelation effect of the fromed phases in the Fe-based MG coating.

Microstructure Examination

Figure 18 shows the SEM image of the microstructure taken at the interface. As shown, all the samples showed crystalline phases embedded in amorphous structure appeared as plain grey surface. Equiaxed grains appeared in all samples which represents the Cr and Fe phases recognized in XRD. In addition, nano-crystals are recognized. However, in samples D1 and E1, a dentritic structure becomes dominant and clear which is referred to $Cr_{23}C_6$ and Fe-Cr-C. A columnar dendritic structure usually is a result of higher cooling rate of multi-element compounds which is present at the interface. It is noticed that the dentritic structure layer is decreasing with the increasing scanning speed [40].

Figure 19 shows the SEM image of the microstructure taken at the coating layer. The samples showed different microstructure from that obtained at the interface. Beside the dendritic structure – coarse and equiaxed – bright square-shaped crystals are existed. As mentioned before, the equiaxed grains appeared represent the soft crystalline phases (Fe and Cr), while the coarse dendritic crystals appeared in sample E1 correspond to $Cr_{23}C_6$ and Fe-Cr-C. The bright square-shaped crystals phases are corresponded to hard intermetallic compounds (B_6Fe_{23}, FeN) [41].

As revealed by SEM pictures, coarse dendritic crystals appeared in sample E1 which exhibited high crystallinity content (18.11%) – as shown in XRD. For samples E2 and E3, the dendritic structure layer becomes smaller and amorphous content increases as the scanning speed is increasing. The samples D1, D2 and D3 showed the same trend as samples E1, E2 and E3.

Although the power density and scanning speed of sample A2 and sample E1 are the same, it is found that sample E1 exhibited higher crystallinity content. This reveals the significance effect of the laser power.

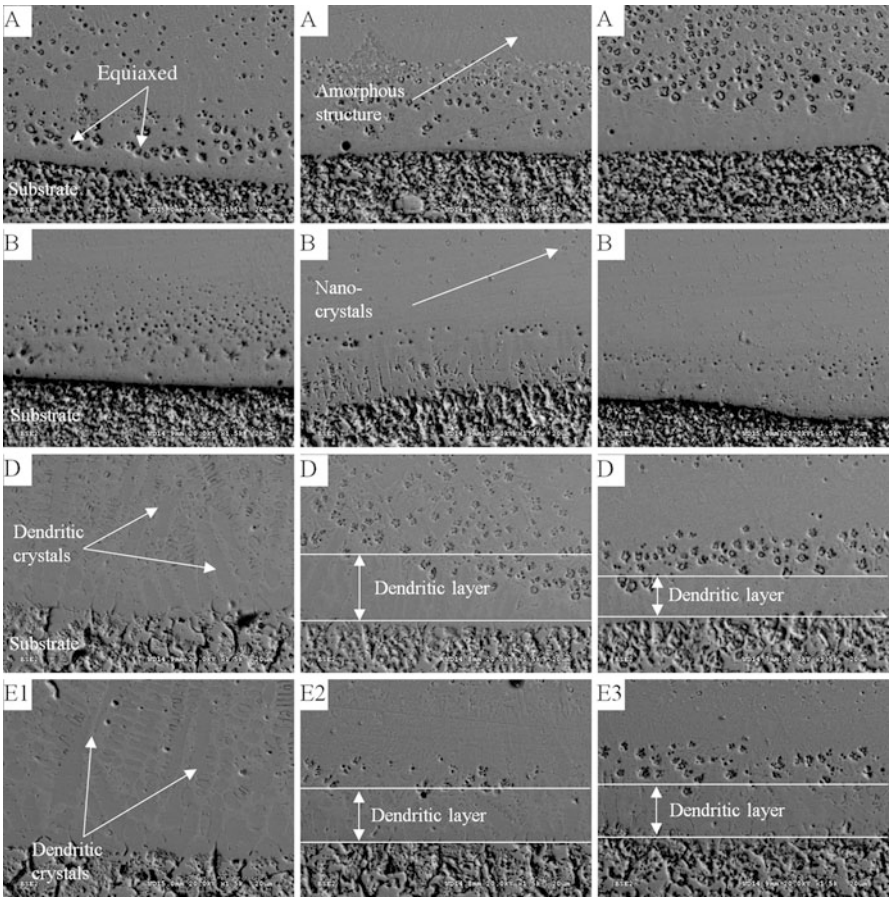

Fig. 18 SEM image at the interface of fabricated samples

It is clear from the microstructure analysis that the laser power and scanning speed affects significantly the types and the shape of formed structure. The multiple phases formed in the samples exhibited different crystalline structure within the interface or the coating layer.

Hardness Measurement

The hardness values in HV0. 1 of the surfaces are shown in Fig. 20. The hardness of the coating exceeded 1300 HV0.1 which is more than 5 times the hardness of the substrate (the substrate hardness is 230 HV0.1). The high value of hardness is referred to the amorphous structure at the coating layer. However, the presence of crystalline phase degrades the hardness depending on the formed phases. For example, samples B1 and B2 exhibited formation of Cr and Fe phases, and the

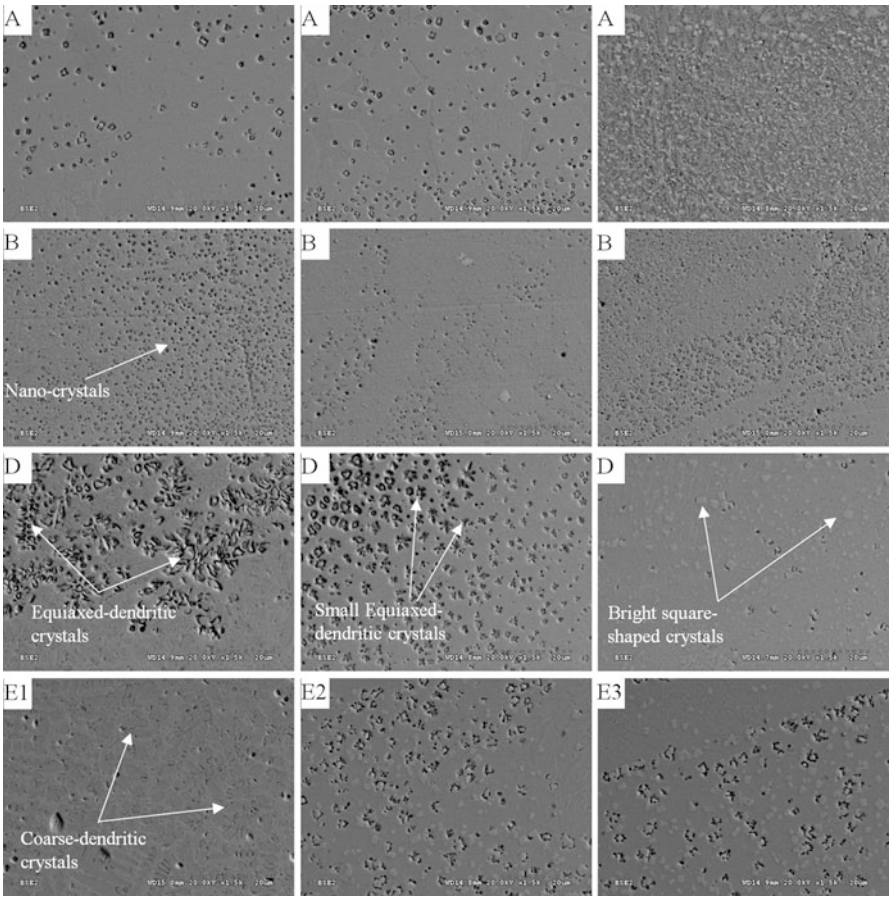

Fig. 19 SEM image at coating layer of fabricated samples

hardness value is dropped below 600 HV0.1. While in samples D1 and E1, $Cr_{23}C_6$ and Fe-Cr-C was the dominant phases. So, the measured hardness was about 900 HV0.1. this can be understood as the carbides are harder than the pure metal phases as Cr and Fe.

For more investigations, a profile hardness value along the cross-section for each sample is revealed in Fig. 21. From the hardness measurement, four layers are found along the cross-section; coating layer (CL), transition layer (TL), heat affected zone (HAZ) and substrate. The CL is featured with high hardness above 1000 HV0.1 which indicates the amorphous structure existence. It is important to mention that all samples exhibited mixed structure at CL which revealed in the microstructure images. That explains why the hardness value is fluctuating in the CL.

The hardness value is dropped (below 800 HV0.1) in the transition layer because of the higher content of crystalline phases. In addition, hard phases – $Cr_{23}C6$, B_6Fe_{23}, Cr-Fe-C, FeN – are found in CL, while Fe and Cr are found in the

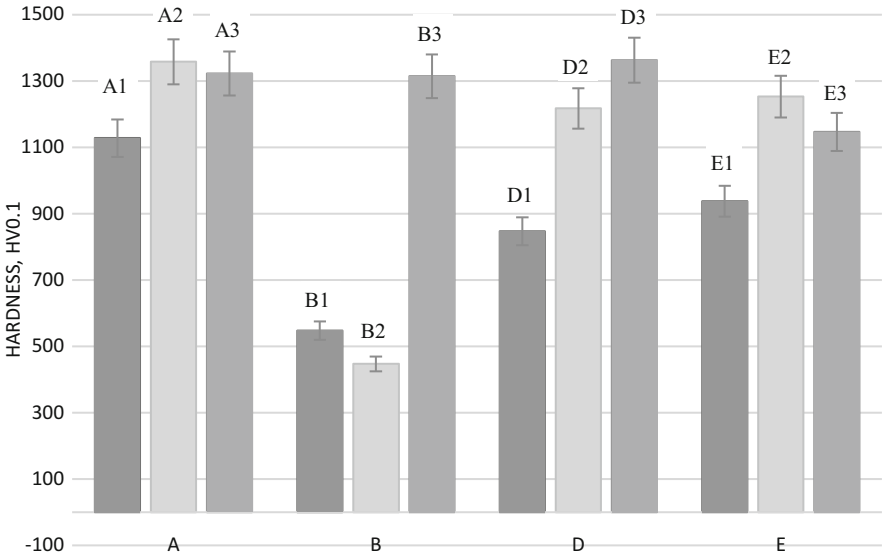

Fig. 20 Surface hardness of Fe-based MG coating

TL. Hence, the resulting hardness of the TL becomes lower than the hardness of the CL. After the TL, HAZ layer – which is in the substrate – is found with hardness value below 500 HV0.1. The HAZ layer depth are variant according to the laser power density and the scanning speed.

It is noticed that both samples D1 and E1 exhibited almost equal hardness value at the CL and the TL with noticeable fluctuation. This result conforms with the XRD and microstructure investigations that showed higher crystallinity content. However, CL and TL hardness still higher than the hardness of HAZ layer due to the formation of hard compounds as well as the amorphous structure.

Electrochemical Corrosion Test

The Potentiodynamic polarization curves for the Cronidur 30 substrate and the amorphous coatings are shown in Fig. 22. Furthermore, the values of corrosion potential (E_{corr}) and corrosion current (i_{corr}) can be estimated from the Tafel slope and are shown in Table 4.

The comparison of the polarization curves indicates that the Fe-based MG coatings have a higher corrosion potential as compared to Cronidur 30. Furthermore, they exhibit a significantly wider passive region. It is noted that samples A2 and D3 exhibited the highest open circuit potential while the sample E2 was the worst compared to the coated samples.

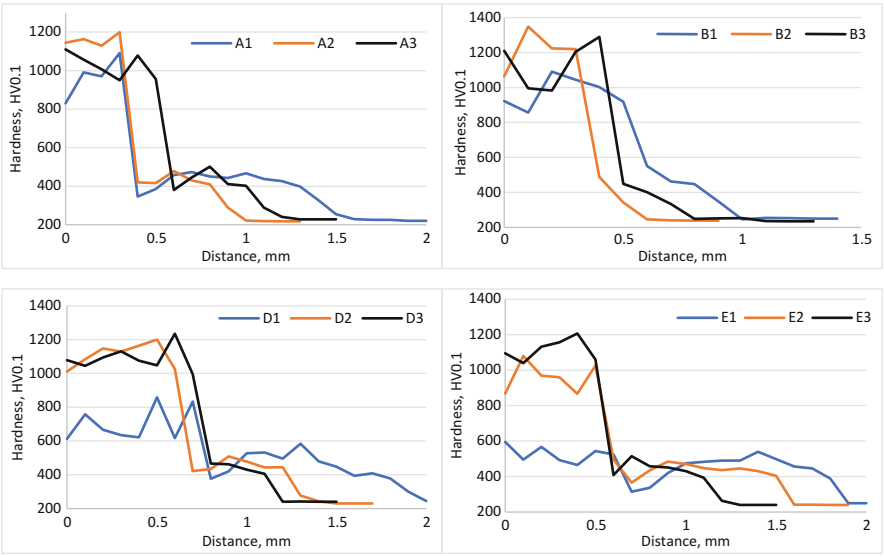

Fig. 21 Profile hardness measured at the cross-section of the fabricated samples

These results correspond to the evaluation of corrosion resistance of the tested samples, i.e. sample A2 exhibited the best corrosion resistance and E2 exhibited the poorest corrosion resistance while samples B3 and D3 lies in-between. From these findings, it can be concluded that amorphous structure found in the Fe-based MG coating affects directly the corrosion resistance level. The excellent corrosion resistance of MGs is referred to the absence of the structure defects as grain boundaries which are weak and corrode rapidly [42].

As all samples exhibited crystalline phases with different percentages, it is noted that lower crystalline percentage showed better corrosion resistance. However, the type of crystalline phases has a significant effect on the corrosion resistance. For example, sample B3 has lower crystallinity content than sample A2, but sample B3 showed lower corrosion resistance. This can be understood from the XRD findings, which showed that hard compounds – $Cr_{23}C_6$ and Fe-Cr-C – were dominant in sample A2 while soft phases – Fe and Cr – were dominant in sample B3 (Table 4).

2.3.4 Conclusion

A successful Fe-based MG layer was developed on stainless-steel substrate using laser cladding technique. The fabricated samples were investigated using XRD, SEM, Micro-hardness and electrochemical corrosion test. The samples showed amorphous structure with different crystallinity content percentages.

The XRD analysis revealed the existence of various compounds as $Cr_{23}C_6$, B_6Fe_{23}, Fe-Cr-C besides pure Fe and Cr crystalline phases. Both the microstructure

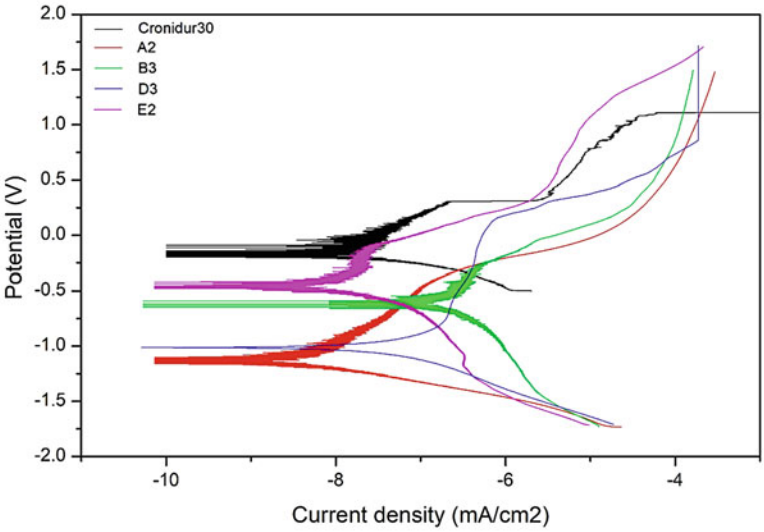

Fig. 22 Potentiodynamic curves of the Cronidur 30 substrate and Fe-based MG coatings in Ringers solution

Table 4 Corrosion potential and current for coated samples and uncoated substrate

Sample	E_{corr} (V)	i_{corr} (mA/cm^2)
Cronidur30	−0.186	−7.8
A2	−0.942	−6.8
B3	−0.462	−6
D3	−0.846	−6.3
E2	−0.407	−7.2

analysis and Micro-hardness measurements confirmed the results obtained from the XRD analysis. The results showed that the amorphous structure as well as the multi-phases recognized affect the corrosion resistance and the hardness. So, the crystallinity content percentage is not the only factor, but also the type of the crystalline phases – hard or soft phases.

It is concluded that the laser power has the strongest effect on the properties of the fabricated coating layer. Also, scanning speed has a significant effect on the crystallinity content percentage. Increasing the scanning speed increases the cooling rate, hence better amorphous structure.

From the hardness measurement and the electrochemical corrosion test results, samples A2 (1500 W, 20 mm/s with spot size 4 × 4 mm) and D3 (4000 W, 40 mm/s with spot size 4 × 6 mm) exhibited the highest hardness value and the best corrosion resistance.

Acknowledgements The authors would like acknowledge Nippon Sheet Glass Foundation (Japan) for the grant provided, Energietechnik Essen GmbH for supplying ASTM F2229 (CORINDUR 30) free sample and LiquidMetal® Coatings for supplying Fe-based amorphous powder as free sample. Also, the authors would like to thank Southern Taiwan University for Science and Technology for providing the necessary facilities and resources to carry out the experimental work. Also, the authors would like to thank both University Malaya and King Fahd University of Petroleum & Minerals for providing financial and technical support.

References

1. Jensen, W. (2018), Production of hip implant by using additive manufacturing Available at: https://www.eos.info/press/case_study/additive_manufactured_hip_implant [Accessed 8 Jun. 2018].
2. M. Z. Ibrahim, A. A. D. Sarhan, F. Yusuf, and M. Hamdi, "Biomedical materials and techniques to improve the tribological, mechanical and biomedical properties of orthopedic implants – A review article," *J. Alloys Compd.*, vol. 714, pp. 636–667, 2017.
3. W. KLEMENT, R. H. WILLENS, and P. DUWEZ, "Non-crystalline Structure in Solidified Gold–Silicon Alloys," *Nature*, vol. 187, no. 4740, pp. 869–870, Sep. 1960.
4. N. Espallargas, R. E. Aune, C. Torres, N. Papageorgiou, and A. I. Muñoz, "Bulk metallic glasses (BMG) for biomedical applications—A tribocorrosion investigation of Zr55Cu30Ni5Al10 in simulated body fluid," *Wear*, vol. 301, no. 1, pp. 271–279, 2013.
5. Y. Waseda and K. T. Aust, "Corrosion behaviour of metallic glasses," *J. Mater. Sci.*, vol. 16, no. 9, pp. 2337–2359, Sep. 1981.
6. A. L. Greer, T. Egami, T. Iwashita, and W. Dmowski, "Mechanical Properties of Metallic Glasses," *Metals (Basel).*, vol. 3, no. 1, pp. 77–113, 2013.
7. S. Wang, "Corrosion Resistance and Electrocatalytic Properties of Metallic Glasses," in *Metallic Glasses - Formation and Properties*, InTech, 2016.
8. J. F. Löffler, "Bulk metallic glasses," *Intermetallics*, vol. 11, no. 6, pp. 529–540, Jun. 2003.
9. A. Peker, W. L. Johnson, and M. Keck, "A highly processable metallic glass: Zr41.2Ti13.8Cu12.5Ni10.0Be22.5," *Cit. Appl. Phys. Lett. Appl. Phys. Lett*, vol. 63, no. 65, pp. 2342–2136, 1993.
10. Y.-L. Gao, J. Shen, J.-F. Sun, G. Wang, D.-W. Xing, H.-Z. Xian, and B.-D. Zhou, "Crystallization behavior of ZrAlNiCu bulk metallic glass with wide supercooled liquid region," 2003.
11. J. Eckert, "Application of amorphous alloys: potential and challenges to overcome."
12. J. Qiao, H. Jia, and P. K. Liaw, "Metallic glass matrix composites," *Mater. Sci. Eng. R Reports*, vol. 100, pp. 1–69, 2016.
13. H. F. Li and Y. F. Zheng, "Recent advances in bulk metallic glasses for biomedical applications.," *Acta Biomater.*, vol. 36, pp. 1–20, May 2016.
14. Q. Chen and G. A. Thouas, "Metallic implant biomaterials," *Mater. Sci. Eng. R Reports*, vol. 87, pp. 1–57, 2015.
15. J. C. Huang, J. P. Chu, and J. S. C. Jang, "Recent progress in metallic glasses in Taiwan," *Intermetallics*, vol. 17, no. 12, pp. 973–987, Dec. 2009.
16. D. F. Williams, "On the mechanisms of biocompatibility," *Biomaterials*, vol. 29, no. 20, pp. 2941–2953, Jul. 2008.
17. X. Lan, H. Wu, Y. Liu, W. Zhang, R. Li, S. Chen, X. Zai, and T. Hu, "Microstructures and tribological properties of laser cladded Ti-based metallic glass composite coatings," *Mater. Charact.*, vol. 120, pp. 82–89, 2016.
18. Y. B. Wang, H. F. Li, Y. F. Zheng, and M. Li, "Corrosion performances in simulated body fluids and cytotoxicity evaluation of Fe-based bulk metallic glasses," *Mater. Sci. Eng. C*, vol. 32, no. 3, pp. 599–606, 2012.

19. J. Schroers, G. Kumar, T. M. Hodges, S. Chan, and T. R. Kyriakides, “Bulk metallic glasses for biomedical applications,” *JOM*, vol. 61, no. 9, pp. 21–29, Sep. 2009.
20. J. A. Horton and D. E. Parsell, “Biomedical Potential of a Zirconium-Based Bulk Metallic Glass.”
21. L. Huang, D. Qiao, B. A. Green, P. K. Liaw, J. Wang, S. Pang, and T. Zhang, “Bio-corrosion study on zirconium-based bulk-metallic glasses,” *Intermetallics*, vol. 17, no. 4, pp. 195–199, 2009.
22. Y. Sun, Y. Huang, H. Fan, Y. Wang, Z. Ning, F. Liu, D. Feng, X. Jin, J. Shen, J. Sun, and J. J. J. Chen, “In vitro and in vivo biocompatibility of an Ag-bearing Zr-based bulk metallic glass for potential medical use,” *J. Non. Cryst. Solids*, vol. 419, pp. 82–91, 2015.
23. R. C. Budhani, T. C. Goel, and K. L. Chopra, “Melt-spinning technique for preparation of metallic glasses,” *Bull. Mater. Sci.*, vol. 4, no. 5, pp. 549–561, Dec. 1982.
24. T. Gheiratmand and H. R. M. Hosseini, “Finemet nanocrystalline soft magnetic alloy: Investigation of glass forming ability, crystallization mechanism, production techniques, magnetic softness and the effect of replacing the main constituents by other elements,” *J. Magn. Magn. Mater.*, vol. 408, pp. 177–192, Jun. 2016.
25. Xue Liang, Jiuhua Chen, Maria Teresa Mora, Jose Fernandez Urdaneta, Qiaoshi Zeng, (2017) Effect of Precipitation on the Hardness of Ternary Metallic Glass. Advances in Materials Physics and Chemistry 07 (06):255–262
26. X. Wang and Xin, “Surface Crystallization in Mg-Based Bulk Metallic Glass during Copper Mold Casting,” *Adv. Mater. Sci. Eng.*, vol. 2014, pp. 1–4, May 2014.
27. T. Zhang, X. Zhang, W. Zhang, F. Jia, A. Inoue, H. Hao, and Y. Ma, “Study on continuous casting of bulk metallic glass,” *Mater. Lett.*, vol. 65, no. 14, pp. 2257–2260, Jul. 2011.
28. C. K. Chua, C. H. Wong, W. Y. Yeong, C. K. Chua, C. H. Wong, and W. Y. Yeong, “Chapter One – Introduction to 3D Printing or Additive Manufacturing,” in *Standards, Quality Control, and Measurement Sciences in 3D Printing and Additive Manufacturing*, 2017, pp. 1–29.
29. B. Dutta, F. H. Froes, B. Dutta, and F. H. Froes, “Chapter 3 – Additive Manufacturing Technology,” in *Additive Manufacturing of Titanium Alloys*, 2016, pp. 25–40.
30. K. V. Wong and A. Hernandez, “A Review of Additive Manufacturing,” *ISRN Mech. Eng.*, vol. 2012, pp. 1–10, Aug. 2012.
31. I. Yadroitsev, A. Gusarov, I. Yadroitsava, and I. Smurov, “Single track formation in selective laser melting of metal powders,” *J. Mater. Process. Technol.*, vol. 210, no. 12, pp. 1624–1631, Sep. 2010.
32. W. E. Frazier, “Metal Additive Manufacturing: A Review,” *J. Mater. Eng. Perform.*, vol. 23, no. 6, pp. 1917–1928, Jun. 2014.
33. R. Udroiu, “Powder Bed Additive Manufacturing Systems and its Applications,” Acad. J. Manuf. Eng., vol. 10, no. 4, pp. 122–129, 2012.
34. C. Leyens and E. Beyer, “Innovations in laser cladding and direct laser metal deposition,” in *Laser Surface Engineering*, Elsevier, 2015, pp. 181–192.
35. R. Liu, Z. Wang, T. Sparks, F. Liou, and J. Newkirk, “13 – Aerospace applications of laser additive manufacturing,” in *Laser Additive Manufacturing*, 2017, pp. 351–371.
36. M. Wai Yip, S. Barnes, and A. Aly Diaa Mohmmed Sarhan, “Deposition of a Silicon Carbide Reinforced Metal Matrix Composite (P25) Layer Using CO_2 Laser,” *J. Manuf. Sci. Eng.*, vol. 137, no. 3, p. 31010, 2015.
37. F. Arias-González, J. del Val, R. Comesaña, J. Penide, F. Lusquiños, F. Quintero, A. Riveiro, M. Boutinguiza, and J. Pou, “Fiber laser cladding of nickel-based alloy on cast iron,” *Appl. Surf. Sci.*, vol. 374, pp. 197–205, Jun. 2016.
38. M. Xu, J. Li, J. Jiang, and B. Li, “Influence of Powders and Process Parameters on Bonding Shear Strength and Micro Hardness in Laser Cladding Remanufacturing,” *Procedia CIRP*, vol. 29, pp. 804–809, 2015.
39. T. Degen, M. Sadki, E. Bron, U. König, and G. Nénert, “The HighScore suite.” Powder Diffraction, p. pp S13-S18, 2014.

40. S. Guo and C. Su, "Micro/nano ductile-phases reinforced Fe-based bulk metallic glass matrix composite with large plasticity," *Mater. Sci. Eng. A*, vol. 707, pp. 44–50, Nov. 2017.
41. M. F. De Carvalho, U. Federal, D. S. Carlos, R. Washington, L. Km, S. P. São, and C. Sp, "LASER CLADDING OF Fe-BASED BULK METALLIC GLASSES," vol. 19, no. April 2017, 2015.
42. R. Li, Z. Li, Y. Zhu, and K. Qi, "Structure and corrosion resistance properties of Ni–Fe–B–Si–Nb amorphous composite coatings fabricated by laser processing," *J. Alloys Compd.*, vol. 580, pp. 327–331, Dec. 2013.